Results in Engineering 14 (2022) 100424

Contents lists available at ScienceDirect

Results in Engineering

journal homepage: www.sciencedirect.com/journal/results-in-engineering

Crushing and energy absorption properties of additively manufactured concave thin-walled tubes

Ahmad Baroutaji [a,b,*], Arun Arjunan [a,b], Gurpal Singh [a,b], John Robinson [a,b]

[a] School of Engineering, University of Wolverhampton, Telford Innovation Campus, TF2 9NT, UK
[b] Additive Manufacturing of Functional Materials Research Group, Centre for Engineering Innovation and Research, University of Wolverhampton, Telford Innovation Campus, TF2 9NT, UK

ARTICLE INFO

Keywords:
Concave tubes
Thin-walled structures
Energy absorption
Quasi-static
Axial loading
Splitting deformation
Crashworthiness
Additive manufacturing
Selective laser melting

ABSTRACT

Developing an innovative protective structure with excellent energy absorption performance is a continuous research effort. The emerging additive manufacturing techniques allow fabricating structures with complex geometrical shapes which have the potential to yield unprecedented energy absorption properties.

Accordingly, in this paper, the crush and energy absorption behaviour of new designs, namely Concave Tubes (CTs) featuring inwardly curved sidewalls, is assessed experimentally and compared to that of Standard tubes (STs) featuring straight sidewalls. Tubes with different geometrical configurations, including concave circular (CC), concave square (CS), standard circular (SC), and standard square (SS), are fabricated using the Selective Laser Melting (SLM) process from AlSi10Mg aluminium powder and then crushed axially under quasi-static loading. It was found that the tubes have fractured and developed a splitting deformation mode, instead of progressive buckling, during the axial crushing resulting in relatively low energy absorption performance. The experimental results revealed superior energy absorption performance for the CTs over the STs. A Multi-Attribute Decision Making (MADM) technique known as Complex Proportional Assessment (COPRAS) is used to identify the best design. The COPRAS results show that the CC design is the best energy absorbing tube outperforming all other configurations presented in this paper.

1. Introduction

Crashworthiness and energy absorption behaviour of protective structures is of particular importance for vehicle design to protect the occupants from serious injuries and to ensure their safety during collision accidents [1]. The conventional thin-walled metallic tubes with simple cross-sections, such as circular and square, have extensively been used as sacrificial protective components to enhance the crashworthy performance. Such components dissipate the impact energy through irreversible plastic deformation; and they also exhibit many advantages such as low cost, ease of manufacturability, lightweight, and excellent energy absorption capacity. In addition to the conventional tubes, more advanced structural components, such as multi-cell [2–4], functionally graded thickness [5,6], nested [7–9], windowed [10], corrugated [11], and foam-filled [12,13] tubes, were also proposed as energy absorbers and they have generally shown enhanced crashworthiness performance compared to the conventional tubes. To fully understand the crushing behaviour and energy absorption mechanism, numerous studies have been carried out using experimental, numerical, and analytical approaches on conventional tubes under various types of loading including axial [14], lateral [15–17], bending [18], and oblique [19–21]. The axially deformed components are the most important elements of any protective structure due to their high energy absorbing potential. The specific energy absorption capacity of axially loaded tubes is almost 10 times greater than the tubes deformed laterally or in bending [22]. The early investigations on axial deformation focused mainly on circular, square and hexagonal tubes with straight sidewalls where many researchers analytically derived mathematical expressions for the average crushing force of these tubes based on the balance of external and internal work [23–25]. It was found that such tubes can absorb energy through progressive buckling deformation mode and their energy absorption capability is a function of the geometrical parameters and material properties. For certain dimensions, the tubes might develop a global bending mode, instead of the progressive buckling, and this mode causes a significant deterioration in their energy absorption performance [26]. Changing the geometry of the tube, i.e. shape and

* Corresponding author. School of Engineering, University of Wolverhampton, Telford Innovation Campus, Priorslee, Telford, TF2 9NT, UK.
E-mail address: ahmad.baroutaji2@mail.dcu.ie (A. Baroutaji).

https://doi.org/10.1016/j.rineng.2022.100424
Received 30 September 2021; Received in revised form 12 April 2022; Accepted 19 April 2022
Available online 22 April 2022

dimension of the cross-section, in the lengthwise direction may alter its crush response and enhance its energy absorption performance. Tubes with lengthwise changed shape, such as tapered tubes and tubes with axial variable thickness (AVT), provide the ability to control the instantaneous crushing force during the axial deformation as the force required to form a fold at a specific axial distance of the tube depends on the geometrical properties at that distance. In particular, the tapered tubes, which have inclined sidewalls, were found to yield better crashworthiness performance than the straight ones as they don't require crush initiators, have less tendency to global bending deformation mode and can operate effectively under oblique loading [27–29]. However, for the same crush space, the tapered tubes absorb less energy than the straight tubes and therefore greater space requirements are needed for the tapered tubes and this has limited their application in vehicles [30,31]. In addition to the tapering configuration, changing the cross-section in the lengthwise direction can be achieved via using concave sidewalls. However, no attempt was made in the literature to examine the crushing and energy absorption responses of such tubes.

The rapid technological developments in the automotive sector, such as electric vehicles, have demanded developing more innovative energy absorbers with novel material and sophisticated geometrical shapes to meet higher engineering requirements. In the past, due to manufacturing restrictions, the experimental investigations on the novel structures with complex shapes were limited where either numerical simulations or analytical tools were used to examine their performance. In recent times, the rapidly emerging Additive Manufacturing (AM) technologies have enabled fabricating advanced structures with unique performance and greater functionality for various engineering applications such as biomedical [32–36], thermal management [37,38], acoustic [39,40], and crashworthiness [41–43]. Among the different AM techniques, SLM is the most attractive one for fabricating metallic components due to its capability of producing high-dense complex--shaped parts from a variety of materials, such as stainless steel, titanium, aluminium, silver, copper, chromium, and nickel [44,45]. Today, many engineering sectors, such as aerospace and motorsport, has started to replace the conventional metal manufacturing processes, such as forging and casting, by SLM [46]. Additionally, SLM is of great interest for offshore and spacecraft industries where shipping spare parts required for maintenance might be challenging [47]. For a successful SLM build, a number of laser and scan parameters, such as laser power, scan speed and scan spacing (hatch distance), should be specified based on the type of powder. The mechanical performance of the SLM structures depends on a wide range of factors such as powder properties, SLM process parameters, as well as post-processing thermal treatment. Therefore, obtaining a product with desirable properties is a challenging and time-consuming task. In the crashworthiness field, SLM was used to develop energy absorption components with advanced geometrical shape, such as functionally graded thickness tubes [5], corrugated tubes [48], bio-inspired sandwich structures [49], hierarchical structures [50–52], internally grooved tubes [53], lattice structures [41,54,55], and Triply Periodical Minimal Surface (TPMS) structures [56,57]. Aluminium, steel, and titanium alloys were the most used materials for fabricating crashworthiness structures.

In this paper, SLM is used to fabricate novel tubes with concave sidewalls for energy absorption applications. The concave tubes have variable cross-sectional dimensions in the lengthwise direction and therefore they have the potential to yield energy absorption advantages similar to those of the tapered tubes. The tubes were made of AlSi10Mg alloys. The crush and deformation performance of the tubes was investigated experimentally and their responses were compared with those of standard straight tubes.

2. Materials and methods

2.1. Samples description

The tubes studied in this paper are Standard Tubes (STs) and Concave Tubes (CTs) with circular and square cross-sections resulting in four different configurations including Standard Square (SS), Standard Circle (SC), Concave Square (CS), and Concave Circle (CC), as shown in Fig. 1. All the tubes have the same height of 150 mm and the same perimeter of 188.5 mm. The thicknesses of the tubes were varied as such they have the same mass of 27.7 g. The thicknesses of STs and CTs are 1 mm and 1.15 mm, respectively. The sidewalls of STs were straight perpendicular to the cross-section while the sidewalls of CTs were inwardly curved with a radius of 500 mm. The selected dimensions of the tubes are within the typical range used for crashworthiness applications.

2.2. Additive manufacturing process

In the current work, AlSi10Mg aluminium alloy powder, with a chemical position as listed in Table 1, was employed to additively manufacture the different CTs and STs. AlSi10Mg alloys have low density and high strength to weight ratio that are beneficial characteristics for developing lightweight energy absorption structures. The powder was laser melted in a commercial EOS M290 SLM system (400 W Yb-fiber laser, 32 A/400 V power supply, F-theta lens, 100 μm focus diameter, and 7000 hPa, 20 m^3/h inert gas supply, and up to 7 m/s scanning speed) [58]. The building process involved the deposition of a 0.03 mm thickness AlSi10Mg powder on the building platform. The building platform was also made of AlSi10Mg and it was heated up to a minimum of 35 °C before starting the building process. Following the application of the powder, a laser beam with a power of 370 W was applied on the powder in particular regions of the bed, corresponding to the cross-section of the part. The powder in these regions melts and then solidifies rapidly creating the first solid layer of the part. The laser scan speed and distance were set as 1300 mm/s and 0.19 mm, respectively. The above-mentioned process parameters were chosen according to the manufacturer datasheet to produce fully dense parts (approx. 99.8%) [59]. After building the first layer, the building platform was lowered and another layer of powder was applied where the laser beam was used again to melt the powder. The laser travel direction was rotated by 67° for each building layer. This process is repeated until the tubes are completed. The different tubes were built in the direction orthogonal to the cross-section to avoid the need for any support structures thereby shortening the building time and minimizing the post-processing requirements. AlSi10Mg is highly susceptible to oxidation and therefore the building took place in an inert environment of argon where the oxygen concentration within the building chamber was kept below 0.1% to minimise oxidation.

Thermal treatment is an indispensable post-processing step for SLM Al alloys, and other metals, to relieve the residual stresses, caused by the fast solidification rates, and dissolve the anisotropy, caused by layer by layer formation, associated with SLM [60,61]. AlSi10Mg can be heat treated using two main procedures including low-temperature annealing treatment or T6 treatment [62]. Recently, other heat treatment protocols such as Hot Isostatic Pressing (HIP), and a combination of HIP and T6 were also applied to AlSi10Mg [62]. In this work, the stress-relieving low-temperature annealing treatment was used. The fabricated tubes, while still on the building platform, were heat-treated at a temperature of 300 °C for a duration of 2 h in an air atmosphere. The aforementioned heat treatment parameters were chosen according to the manufacturer's recommendations [5,63]. The heat treatment was conducted before removing the building parts from the platform to avoid any possible deformation or cracking to the samples.

As the last step of creating the samples, Wire Electric Discharge Machine (WEDM) was used to remove the tubes from the building

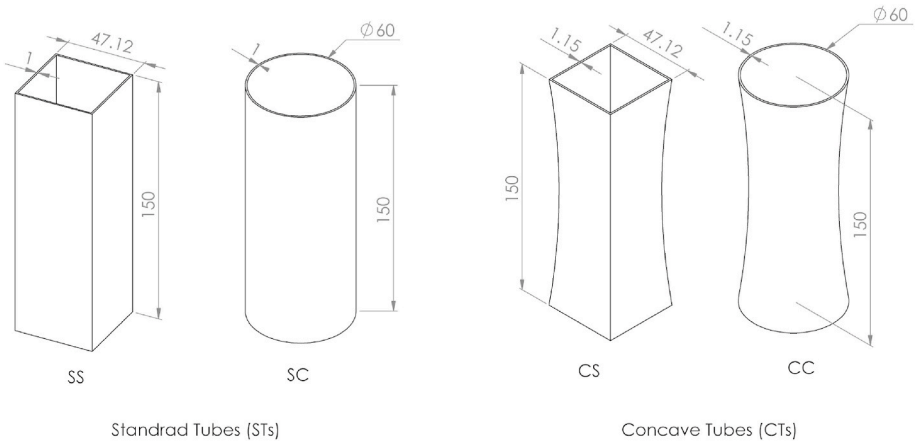

Fig. 1. Geometrical configurations of standard and concave tubes.

Table 1
Material composition of AlSi10Mg (wt. %).

AlSi10Mg										
Al	Si	Fe	Cu	Mn	Mg	Ni	Zn	Pb	Sn	Ti
Bal.	9–11	0.055	0.05	0.45	0.2–0.45	0.05	0.1	0.05	0.05	0.15

platform. During WEDM, the tubes were submerged in water and therefore they were air-blasted to dry after removing them from the WEDM machine. The surfaces of the manufactured tubes were discoloured, as can be seen in Fig. 2, indicating oxidation and formation of aluminium oxides during the WEDM process.

To evaluate the dimensional accuracy of the printed samples, their geometric dimensions were checked using a digital calliper and a digital micrometre. In-plane thickness measurements were conducted at several locations around the samples' ends. The side length and the diameter of the square and circular tubes were also checked at several locations along the length of the sample. The dimensional accuracy of the printed samples was very good where the actual dimensions of the printed samples were in excellent agreement with the design values exhibiting very small percentage errors.

2.3. Mechanical properties

To determine the mechanical properties of the AlSi10Mg, uniaxial quasi-static tensile tests were conducted on standard flat dog-bone shaped specimens with a gauge length of 35 mm and a thickness of 5.4 mm. The tensile samples were additively manufactured and heat-treated using the same settings adopted for fabricating the CTs and STs tubes. The samples were fabricated in the XY direction with the sample's long axis aligned perpendicular to the building direction as shown in Fig. 3 (a). All the tensile samples were tested at room temperature where they loaded at a rate of 2 mm/min using Zwick-1474.

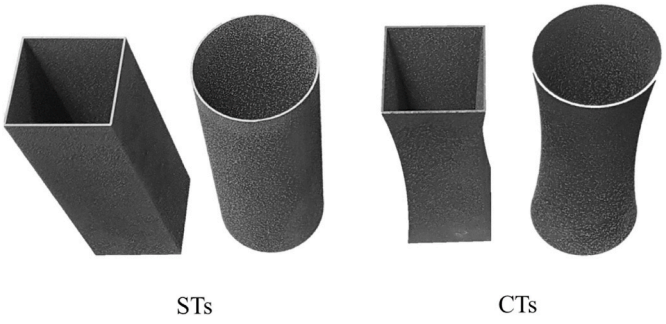

Fig. 2. The SLM-printed CTs and STs samples.

Fig. 3 displays the true stress-strain curves of three tests. These curves were used to extract the mechanical properties of AlSi10Mg. The average yield stress, ultimate tensile strength, and strain to failure were 219.5 MPa and 331 MPa and 0.1, respectively. It is clear that the printed samples in this work exhibit low values of strain to failure indicating a low ductility of the SLM AlSi10Mg.

2.4. Compression test

Fig. 4 shows the setup of the axial compression tests which were conducted using Zwick-1474 universal materials testing machine under quasi-static loading conditions. The machine is floor-standing equipment driven by a 4 kW AC servo-motor and equipped with a loading cell of 100 kN maximum capacity. The maximum and minimum speeds of the machine's crosshead are 0.01 mm/min and 500 mm/min, respectively. During the testing, the samples were placed between the crossheads of the machine and then loaded where the lower crosshead moved vertically upward at a rate of 10 mm/min pressing the samples onto the upper crosshead. All the tubes were crushed up to 80% of the total length resulting in an overall crushing distance of 120 mm. A video recorder was used to capture the deformation history of the samples during the crushing process and the load-displacement responses of the different tubes were recorded by the testing system at a rate of 0.1 ms. The crushing tests were conducted on two samples of each tube to ensure the repeatability and reliability of the experimental observations.

2.5. Crashworthiness metrics

Evaluating the energy absorption performance of the axially loaded CTs and STs can be obtained through calculating some indicators such as Specific Energy Absorption (SEA), Peak Crush Force (PCF), Mean Crush Force (MCF), and Crush Force Efficiency (CFE). Such indicators allow for quantifying the energy absorption characteristics of the structures and they have been widely used in the literature [10].

The energy absorbed per unit mass (SEA) is the most important metric indicating the energy absorption efficiency and allowing for comparing different structures that have different masses. It is an

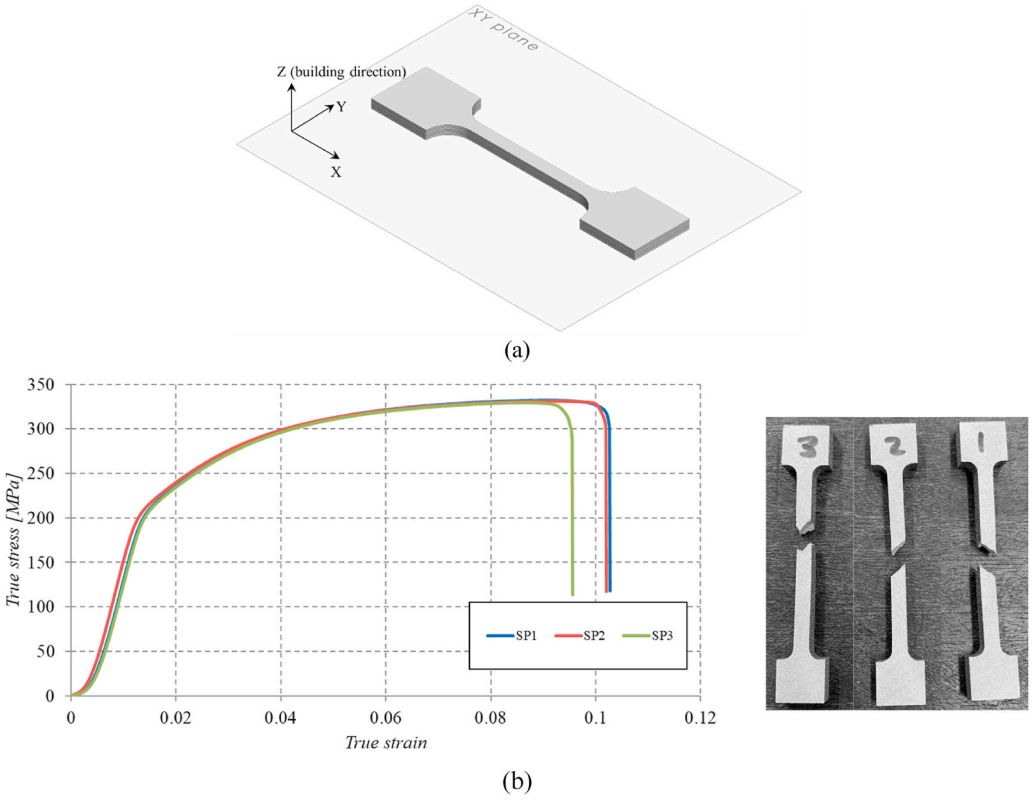

Fig. 3. (a) The building directions of dog-bone specimens (b) True stress-strain responses of AlSi10Mg fabricated via SLM.

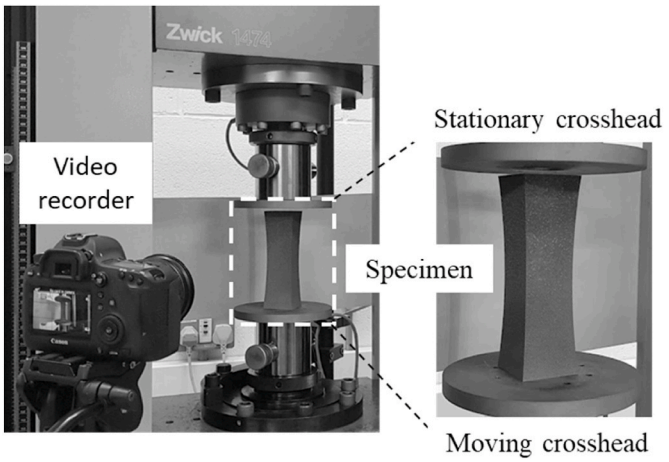

Fig. 4. Compression test set-up.

important design parameter in mass restricted and lightweight applications. A greater SEA implies higher energy absorption efficiency and means that most of the structure's material contributes to the energy dissipation process. SEA can be calculated according to Eq (1):

$$SEA = \frac{EA}{m} \tag{1}$$

where EA is the energy absorbed by the tube during the crushing process and it can be calculated as the area enclosed by the force-displacement curve. Given that F(x) is the instantaneous crushing force at crushing distance x; and δ is the total crushing distance, the mathematical expression of EA can be written as shown in Eq. (2):

$$EA = \int_0^{\delta} F(x)dx \tag{2}$$

PCF is the peak force recorded during the crushing process and it is another important response in the crashworthiness design to ensure the safety of passengers. High PCF levels can cause significant acceleration during a crushing scenario leading to serious damage to the occupants therefore PCF value should not exceed a threshold limit.

MCF is the average crush force over the total crushing distance and it can be obtained based on Eq. (3)

$$MCF = \frac{EA}{\delta} \tag{3}$$

CFE is the ratio of MCF to PCF and it is calculated using Eq. (4)

$$CFE = \frac{MCF}{PCF} \tag{4}$$

A greater CFE indicates a lower PCF with respect to MCF which is a desirable feature for an energy-absorption structure.

In summary, a good energy absorption performance is associated with high SEA, CFE, MCF and low PCF.

2.6. Complex proportional assessment (COPRAS)

The effective energy absorption design is the one that yields high SEA, high CFE, and low PCF. However, such desirable responses often conflict with each other where the high SEA is normally associated with high PCF. Therefore, multi-attribute decision making (MADM) techniques, such as Technique of Order Preference Similarity to the Ideal Solution (TOPSIS), Preference Ranking Organization Method for Enrichment Evaluations (PROMETHEE), Analytical Hierarchy Process (AHP), and Complex proportional assessment (COPRAS), are normally employed to identify the best design among several potential

candidates. In the current study, COPRAS was used to determine the tube with the best combination of energy absorption responses due to its simplicity. The four tubes investigated in this paper were considered as design alternatives within COPRAS framework where they are ranked based on their relative significance concerning the energy absorption performance criteria. The full implementation of COPRAS for designing an energy absorption structure is detailed below.

Step 1: Develop an initial decision matrix X.

The first step in implementing COPRAS is to establish an initial decision matrix X mapping the candidates, i.e. the tubes, to their attributes, i.e. energy absorption responses. The matrix X can be expressed as

$$X = \left[x_{ij}\right]_{mn} = \begin{bmatrix} x_{12} & x_{12} & .. & x_{1n} \\ x_{21} & x_{22} & .. & x_{2n} \\ .. & .. & .. & .. \\ x_{m1} & x_{m2} & .. & x_{mn} \end{bmatrix} \quad (5)$$

where m and n are the number of the candidates and the number of attributes, respectively. Thus, x_{ij} represents the performance of the i_{th} tube in terms of the j_{th} attribute.

Step 2: Generate a normalized decision matrix R.

Since the different design attributes have different units, they can not be compared directly to each other and this makes the selection process much harder. Therefore, the matrix X should be converted into a nondimensional one to make the design attributes comparable. The nondimensional, normalized, decision matrix R is formulated as

$$R = \left[r_{ij}\right]_{mn} = \frac{x_{ij}}{\sum_{i=1}^{m} x_{ij}} \quad (6)$$

where r_{ij} denotes the normalized j_{th} attribute for i_{th} design.

Step 3: Compute the individual weightage of each attribute. w_j

The w_j for each attribute can be found as follows.

- First, every two attributes need to be compared at a time. This will result in a total number of comparisons equal to $N = (n(n-1)/2)$. When the compared attributes are of different importance for the selection process, a score of 3 should be assigned to the more important attribute while a score of 1 should be given to the less important attribute. On the other side, if the compared attributes are equally important for the selection process, then a score of 2 can be assigned to both of them.
- Second, following the comparison, the total score for each attribute can be obtained as

$$W_j = \sum_{i=1}^{N} w_{ij} \quad (7)$$

- Third, the weightage of the j_{th} attribute can be obtained by dividing the total score of each attribute W_j by the global total score G

$$w_j = \frac{W_j}{G} = \frac{W_j}{\sum_{j=1}^{n} W_j} \quad (8)$$

Step 4: Determine the weighted normalized decision matrix D.

Matrix D can be obtained by multiplying the normalized matrix R by the individual weightage of each attribute and it can be written as shown in Eq. (9)

$$D = \left[y_{ij}\right]_{mn} = r_{ij} \times w_j \quad (9)$$

where y_{ij} is the weighted normalized j_{th} attribute for i_{th} design.

Step 5: Find the summation of the beneficial and non-beneficial attributes for each design alternative.

The matrix D contains both beneficial and non-beneficial attributes denoted as $+y_{ij}$ and $-y_{ij}$, respectively. The good design candidate is the one that has a greater value for the beneficial attributes and a smaller value for non-beneficial attributes. Therefore, for each design alternative the summation of the beneficial (S_{+i}) and non-beneficial (S_{-i}) attributes should be obtained as shown in Eqs. (10) and (11)

$$S_{+i} = \sum_{j=1}^{n} +y_{ij} \quad (10)$$

$$S_{-i} = \sum_{j=1}^{n} -y_{ij} \quad (11)$$

Step 6: Determine the minimum value of S_{-i} which can be written as

$$S_{-min} = \min S_{-i} \quad (12)$$

Step 7: Calculate the relative significance (Q_i) and the quantitative utility (U_i) for each design alternative.

Q_i and U_i are the main measures obtained as a result of applying COPRAS and they are used to determine the priority of the design candidates in terms of meeting the selection criteria. They can be calculated using Eq. (13) and Eq. (14)

$$Q_i = S_{+i} + \frac{S_{-min} \times \sum_{i=1}^{m} S_{-i}}{S_{-i} \times \sum_{i=1}^{m} (S_{-min}/S_{-i})} \quad (13)$$

$$U_i = \frac{Q_i}{Q_{max}} \times 100 \quad (14)$$

The good design alternative is the one that has the maximum values of Qi and Ui. The Ui value can be used to rank the candidates where the candidate with the maximum Ui is ranked first while the candidate with the minimum Ui is ranked last.

3. Results and discussion

3.1. Crush behaviour and deformation mode

Fig. 5 and Fig. 6 depict the force-displacement curves while Fig. 7 displays the deformation stages for all STs and CTs as obtained from the axial crushing tests. The tubes were crushed up to 80% of their original lengths (i.e. 150 mm).

The force-displacement characteristics of all tubes exhibit a rapid increase in the crushing forces to the first peak values which correspond to the forming of the first wrinkle, i.e. buckling path, in the tube triggering the start of the plastic deformation process. The concave tubes, both CC and CS, required greater forces to initiate the crushing compared to their standard counterparts, i.e. SC and SS. Following the initial buckling response, the crushing force abruptly drops to lower levels. The typical post-buckling stage of an axially loaded tube features a repeated pattern of fluctuations in the axial force corresponding to the development of a series of sequential wrinkles and progressive folding in the tube. Inspecting the post-buckling stage of the CTs and STs investigated in this paper show a different trend from the typical one.

For SS tubes, it is clear that the tubes show no fluctuations in the post-collapse stage indicating that no successive folding occurs during the crushing. The SS tube was initially deformed by forming one inextensional lobe around its mid-height where two sides of the tube were moved inward, into the cavity of the tube, and the other two sides moved outward. However, the tube material in the lobe zone was fractured along the whole circumferential hoop before developing into a complete fold resulting in a loss of bearing capacity. This fracture is due to the low ductility of the SLM structures which prevents the excessive plastic bending required for the folding process. The occurrence of the fracture within the tube has stopped the desirable progressive folding process and led to a more local tearing within the tube in the region around the first fold. As the tube is compressed further, the buckling mode transforms to a splitting mode where the initial fractured fold served as a “shaped die” causing more tearing and separation of the tube’s materials as can be seen from Fig. 4. The separated sections of the

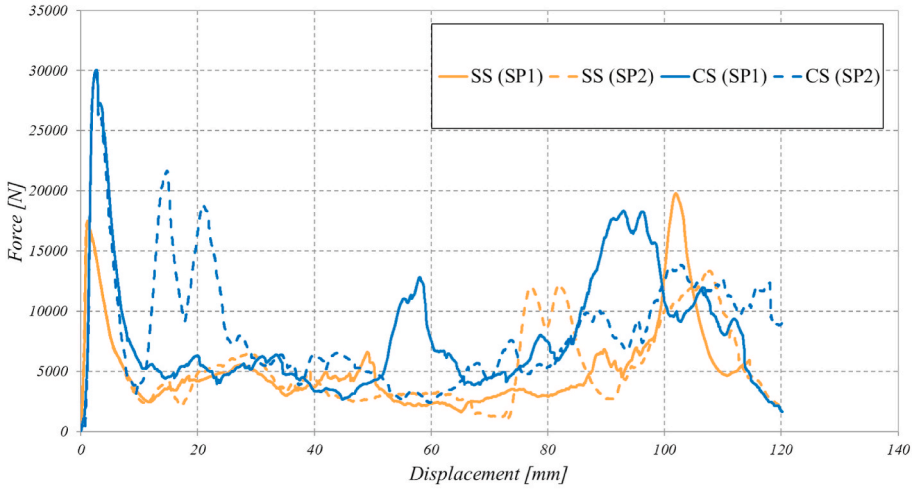

Fig. 5. Force-displacement responses of SS and CS tubes.

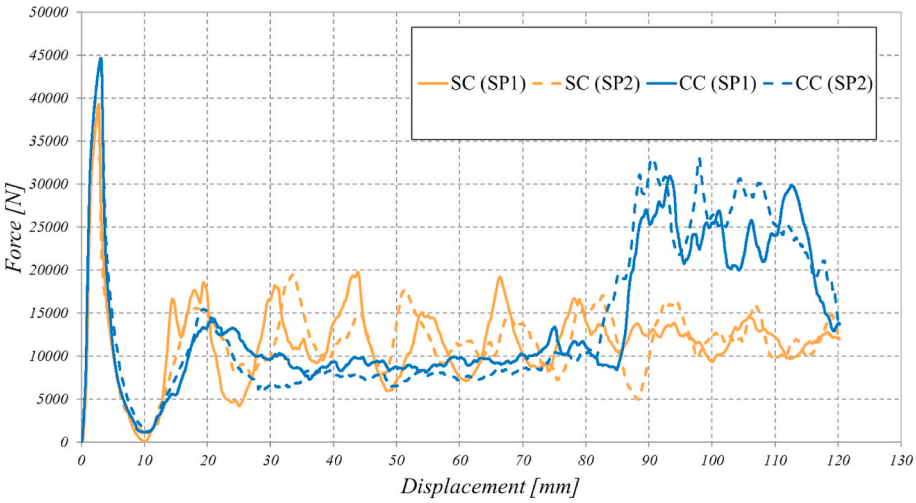

Fig. 6. Force-displacement responses of SC and CC tubes.

tube then interacted with the loading platens and deformed plastically resulting in an increase in the crushing forces as it can be observed from Fig. 5 at crushing displacements of 103 mm and 78 mm for SS(SP1) and SS(SP2), respectively. The crushing force was almost constant for the majority of the post-bucking stage in the SS due to the tube's fracture and absence of folding process. This flat force-displacement response can be considered as an advantage for the energy absorption applications as it allows for constant deceleration and reduced damage or injury during a collision event [64]. The splitting deformation mode is the dominant one for SS tube and only one incomplete fold was generated.

The concave square specimens, i.e. CS tube, have also shown a similar trend to SS tube. The tubes were initially buckled at one of their ends resulting in a peak crush force. During the forming of the first fold, the tube's material was fractured around the buckling path and the crushing force dropped abruptly. Following the fracture, the tube's material started to split and tear and the separated parts have deformed upon contacting with the compressing platens resulting in some loading peaks in the post-buckling stage such as the force peaks observed at around 15 mm and 90 mm crushing displacement for CS2 and CS1, respectively.

From Fig. 6, it can be seen that the SC tubes display a progressive buckling deformation mode. Upon loading of SC tubes, the crushing force increased monotonically to its peak value where the tube started to deform plastically via axisymmetric buckling at its lower end, which is in contact with the moving loading platen. During this stage, the tube's wall bends around the circular hinge lines and stretch circumferentially. After reaching the peak value, the crushing force drops to almost zero indicating a complete fracture of the first fold. The post-buckling performance of SC specimens is very close to the typical one showing some repeated force peaks which correspond to the progressive buckling and folding during the crushing. The SC tubes maintained the progressive buckling where each of the formed folds was eventually fractured along the circumferential hoop of the cross-section. Due to the fracture, the force peaks in the post-buckling stage are much lower than the typical response without fracture. The cracks generated during the crushing of an SLM part are directly linked to its porosity which in turn is influenced by the SLM process parameters [47].

For CC specimens (Fig. 6), the crushing force reached the peak level during the initial buckling but then directly dropped when they started to crack and fracture at different locations around the circumference. As the loading platen continues to compress the tube, the fractured region of the tube served as a 'shaped die' causing tearing for the unreformed regions of the specimens. At this stage, the deformation modes of the tubes transformed from buckling to splitting. The splitting deformation takes place at almost a constant force level and during this stage the tube's material tears creating strips. At crushing displacement of 85 mm,

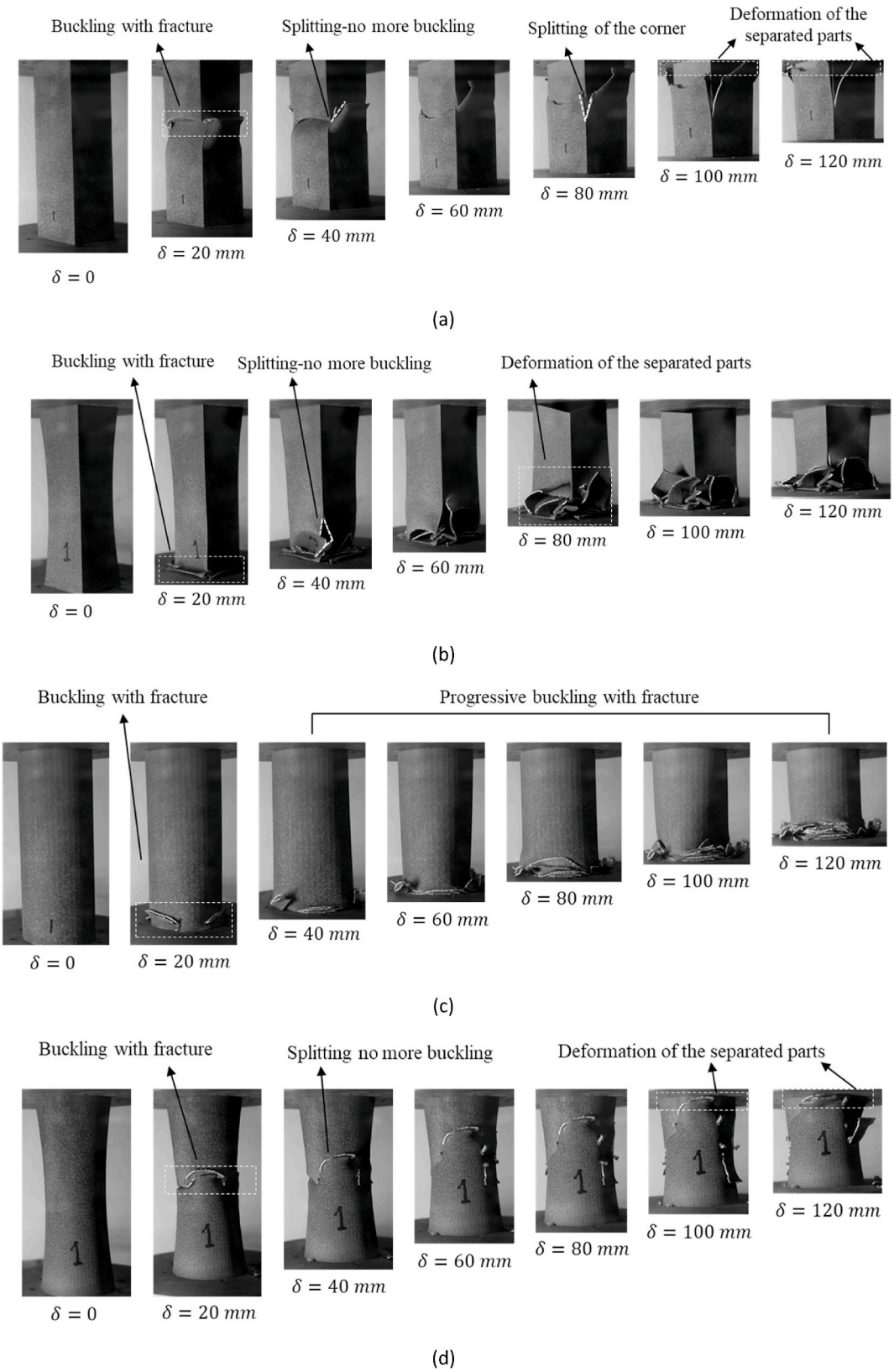

Fig. 7. Deformation modes of (a) SS (b) CS (c) SC (d) CC tubes.

the split sections of the tubes started to deform and fracture upon contacting with the loading platen causing an increase in the crushing force.

All the investigated samples in this study were fractured during the crushing process which led to limited plastic deformation and unfavourable energy absorption performance. The tubes' fracture took place at the location of the first fold generated during the axial crushing. In the current study, no factitious trigger or crush initiator is introduced to the tubes and therefore the first folds, i.e. initial fracture regions, were

developed at random locations in the different tubes. The CC and SS tubes fractured at their middle height while CS and SC fractured at their lower ends which are in contact with the moving crossheads. Generally, the cracks form in the weak zones of the specimens which are subjected to excessive deformation and contain material defects. In the SLM process, material defects, such as internal pores, are common and may appear during the building of any layer of the part influencing its mechanical properties. Therefore, the initial fracture regions of the investigated laser melted tubes were random and sensitive to the material's defects associated with the SLM process.

The fracture of the SLM tubes is well reported in previous studies. Our previous investigation on the lateral collapse of SLM AlSi10Mg circular tubes has reported cracks forming in the weak zones of the tubes [5]. Yang el al [53]. noticed fractures and cracks forming during the axial compression of SLM 316 L circular tubes. Mohamed et al. [65] also observed tearing during the axial crushing of SLM AlSi10Mg tubes. However, the majority of samples examined by Ref. [65] have maintained progressive folding deformation mode despite the cracking. Cracks and fractures of SLM manufactured structures undergoing large deformation are closely linked to the nature of the SLM process and the associated residual stresses that may promote cracks' initiation and propagation. Heat treatment is normally adopted to reduce the influence of the residual stresses. For this work, the SLM process parameters and the heat treatment protocol were chosen based on the manufacturer recommendation to achieve a fully dense part.

Overall, from the obtained results, one can conclude that there is a need to optimise the SLM parameters and environment as well as the subsequent heat treatment for enhancing the ductility of the produced tubes and making them more suitable for crashworthiness applications.

3.2. Energy absorption evaluation

The energy absorption indicators namely; SEA, PCF, MCF, and CFE of the different standard and concave tubes were plotted in Fig. 8. The force-displacement curves, discussed in the previous section, were used to extract the crashworthiness metrics, according to equations stated in section 2.4, where all the metrics were calculated up to a crushing distance of 120 mm.

In terms of SEA, the circular tubes outperform the square counterparts as CC tube exhibits the highest SEA value of 60.64 J/kg which is 168% greater than the SEA of SS which absorbed the lowest amount of energy. The energy absorption superiority of the circular tubes over the square ones is consistent with the literature [1,66,67]. Such trend is due to the fact that the circular tubes absorb energy through both bending and membrane deformations while the square tubes experience severe deformation within limited regions at the corners. As another observation, the concave tubes absorbed greater energy per unit mass than the standard tubes with CC and CS showing 19% and 60% greater SEA than SC and SS, respectively. The good SEA performance of the CTs could be attributed to the plastic deformation of the tubes' strips which were generated during splitting deformation mode. Also, CTs have greater thicknesses than the STs meaning that they have more material in the deformation and fracture zones to participate in the energy dissipation process.

For PCF response, it is clear that the CTs demonstrate higher PCF values than the STs. The PCF of CC and CS tubes are 13.14% and 60.84% greater than SC and SS, respectively. Generally, the PCF value of the axially loaded structures indicates the initiation of the folding process and it normally depends on the elastic stiffness of the structure [68]. In this study, the greater PCF values of CTs are due to fact that they have greater thicknesses compared to STs and therefore they have higher elastic stiffness and require greater force to develop the initial buckling.

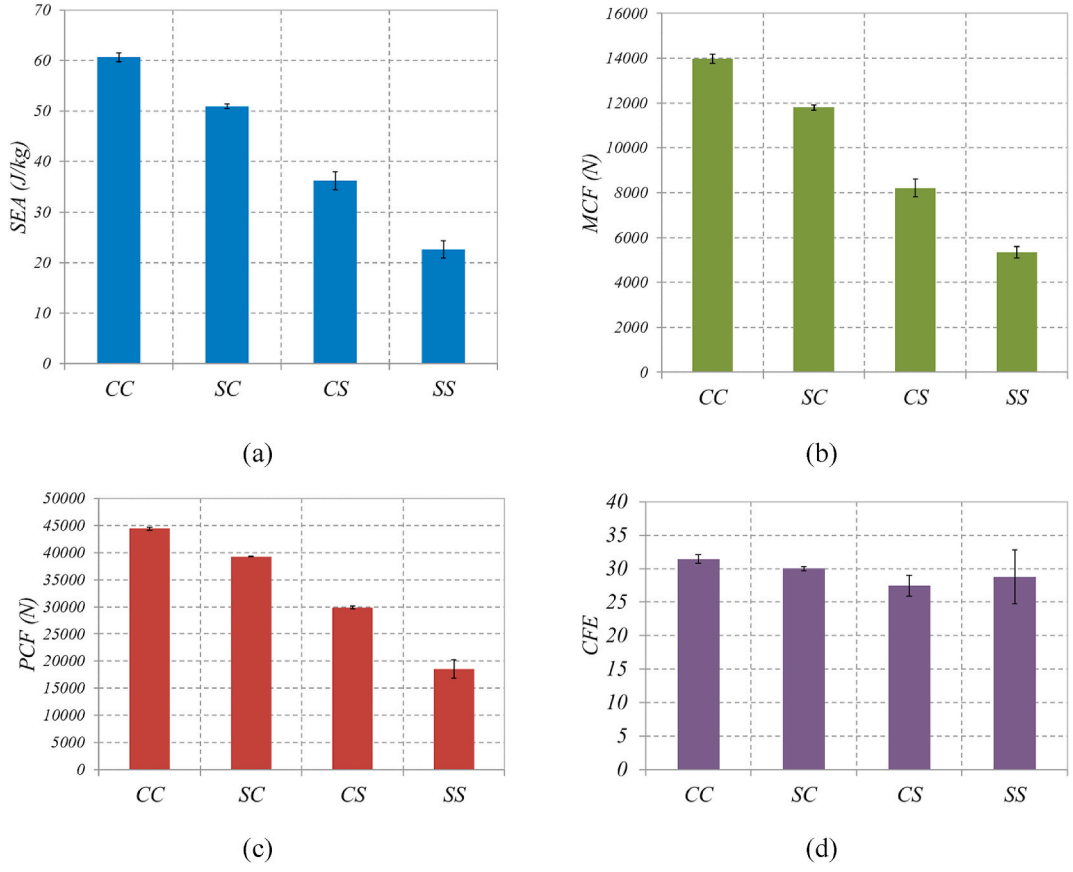

Fig. 8. Crashworthiness metrics of STs and CTs: (a) SEA; (b) MCF, (c) PCF, (d) CFE.

By comparing the circular tubes with the square tubes, it can be seen that the former yields greater PCFs than the latter. CC and SC tubes exhibit 48.7% and 111.4% greater PCF than CS and SS, respectively.

Since the crashworthiness metrics of all tubes were calculated up to the same crushing distance (i.e. 120 mm), MCF results were found to show a similar trend to the SEA. MCFs of CTs are greater than those of the STs. Likewise, MCF of circular tubes is higher than that of square counterparts.

In terms of CFE response, it can be seen that all tubes exhibit similar CFE values with a slight advantage for the CC tube over the other tubes. The CC tube exhibits 4.7%, 14.57%, and 9.38% greater CFE than the SC, CS, and SS tubes, respectively. It was shown before that the MCF and PCF responses follow the same trend meaning that the structures with high MCF have also high PCF which results in balancing the CFE for all tubes. The maximum CFE value recorded for the tubes investigated in this study is 31.45% which is lower than that of standard tubes made of a ductile material and crushed axially. For example, Sun et al. [69] reported a CFE of 37% for an aluminium circular tube with 1 mm thickness, 58 mm diameter, and 150 mm length deforming progressively in a diamond mode. The CFE response can be highly improved by applying a crush trigger to reduce the PCF values [70]. Another way to improve the CFE is to use corrugated tubes instead of straight tubes. Alkhatib et al. [48] found that the SLM corrugated tubes can reduce the PCF achieving a CFE of around 94%.

3.3. Determining the best performing tube

The COPRAS decision matrix, shown in Table 2, consists of the four design alternatives, including CC, CS, SC, and SS tubes, and three attributes detailing their energy absorption responses including SEA, CFE, and PCF. The individual weightage of SEA, PCF, and CFE were determined according to the procedure explained in section 2.6. SEA and PCF were considered more important than CFE for the selection process and therefore they were assigned a score of 3 when compared with CFE and a score of 2 when compared to each other. The process of identifying the individual weightage is detailed in Table 3. The weight normalized, i.e. non-dimensional, decision matrix was obtained according to Eq. (9) and presented in Table 4. To determine S_{+i} and S_{-i}, SEA and CFE were considered as benefical responses whereas PCF was set as non-benefical attribute. Following that, the values of Q_i and U_i for each tube were determined using Eqs. (13) and (14), respectively, and presented along with the rank of the tubes in Table 5. According to the COPRAS results, CC and CS tubes were ranked first and last, respectively. Therefore, CC is the best performing energy-absorbing structure while CS is the worst one among those investigated in the current paper.

4. Conclusion

In this paper, innovative designs of thin-walled tubes with inwardly curved sidewalls, namely concave tubes, were examined for crashworthiness applications under axial loading. The tubes were fabricated from AlSi10Mg alloys using SLM technique. Quasi-static axial crushing tests were conducted on the different specimens to evaluate their crush and energy absorption characteristics and the performance was compared against standard tubes with straight sidewalls.

The laser melted concave and standard tubes have all fractured during the crushing process. The standard circular tube exhibited a mixed deformation mode of progressive folding and fracture while the other tubes have all shown a splitting deformation mode in which the first-formed fold acted as a 'shape die' causing tearing to the remaining sections of the structure without any indication for progressive buckling. Such deformation modes resulted in lower energy absorption performance than the one expected from the typical axially loaded tubes with progressive buckling deformation mode. Generally, the fracture of the tubes is due to the brittleness and low ductility of SLM AlSi10Mg. According to the measured energy absorption metrics, the concave circular (CC) tube was the most efficient structure exhibiting the highest specific energy absorption of 60.64 J/kg and highest crush force efficiency of 31.46%. Based on the obtained results, it is obvious the SLM process doesn't yield the mechanical properties suitable for energy absorption applications and therefore there is a need to improve the elongation and ductility of the manufactured material by optimizing the SLM process and the thermal treatment.

The current work is a preliminary investigation into the feasibility of CTs for crashworthiness applications. Further parametric analysis and geometrical optimisation are still required to reveal the full benefits of such tubes.

Table 2
Initial decision matrix X for COPRAS.

Tube	Attributes		
	PCF [N]	SEA [J/kg]	CFE [%]
CC	44443.46	60.65	31.46
SC	39279.64	50.94	30.04
CS	29889.12	36.21	27.46
SS	18582.89	22.62	28.76

Table 3
Weightage setting for each energy absorption response.

	$N = \frac{n(n-1)}{2} = \frac{3(3-1)}{2} = 3$		
	PCF	SEA	CFE
w_{ij}	2	2	
	3		1
		3	1
Wj	5	5	2
G	12		
wj	0.4166667	0.416667	0.166667

Table 4
Weighted normalized decision matrix.

Tube	PCF	SEA	CFE
CC	0.140082	0.148281	0.044543
SC	0.123806	0.124539	0.042528
CS	0.094208	0.088538	0.038875
SS	0.058572	0.055308	0.040721

Table 5
COPRAS results in terms of Qi and Ui values.

Tube	Qi	Ui	Rank
CC	0.262	1	1
SC	0.246	0.937	3
CS	0.231	0.879	4
SS	0.262	0.999	2

Credit author statement

Ahmad Baroutaji: Conceptualisation, Supervision, Methodology, Software, Investigation, Validation, Formal analysis, Writing original draft, Writing- Reviewing and Editing. Arun Arjunan: Conceptualisation, Supervision, Methodology, Software, Investigation, Validation, Formal analysis, Writing original draft, Writing- Reviewing and Editing. Gurpal Singh: Investigation, Formal analysis, Writing- Reviewing and Editing. John Robinson: Methodology, Investigation, Formal analysis, Writing original draft, Writing- Reviewing and Editing.

Declaration of competing interest

On behalf of co-authors, I can certify that there is no actual or potential conflict of interest in relation to this submission.

Acknowledgement

The authors would like to thank Mr Paul Bates, Mr Neil Basini, and Mr Andrew Gloud for their technical support in the SLM fabrication and mechanical testing. This research was conducted with support from the University of Wolverhampton.

References

[1] A. Baroutaji, M. Sajjia, A.-G.G. Olabi, On the crashworthiness performance of thin-walled energy absorbers: recent advances and future developments, Thin-Walled Struct. 118 (2017) 137–163, https://doi.org/10.1016/j.tws.2017.05.018.
[2] T. Tran, A. Baroutaji, Crashworthiness optimal design of multi-cell triangular tubes under axial and oblique impact loading, Eng. Fail. Anal. 93 (2018) 241–256, https://doi.org/10.1016/J.ENGFAILANAL.2018.07.003.
[3] T.N. Tran, A. Baroutaji, Q. Estrada, A. Arjunan, H. Le, N.P. Thien, Crashworthiness analysis and optimization of standard and windowed multi-cell hexagonal tubes, Struct. Multidiscip. Optim. 63 (2021) 2191–2209, https://doi.org/10.1007/s00158-020-02794-y.
[4] S. Wu, G. Zheng, G. Sun, Q. Liu, G. Li, Q. Li, On design of multi-cell thin-wall structures for crashworthiness, Int. J. Impact Eng. 88 (2016) 102–117, https://doi.org/10.1016/j.ijimpeng.2015.09.003.
[5] A. Baroutaji, A. Arjunan, M. Stanford, J. Robinson, A.G. Olabi, Deformation and energy absorption of additively manufactured functionally graded thickness thin-walled circular tubes under lateral crushing, Eng. Struct. 226 (2021) 111324, https://doi.org/10.1016/J.ENGSTRUCT.2020.111324.
[6] G. Sun, X. Tian, J. Fang, F. Xu, G. Li, X. Huang, Dynamical bending analysis and optimization design for functionally graded thickness (FGT) tube, Int. J. Impact Eng. 78 (2015) 128–137, https://doi.org/10.1016/j.ijimpeng.2014.12.007.
[7] T.N. Tran, D.H. Le, A. Baroutaji, Theoretical and numerical crush analysis of multi-stage nested aluminium alloy tubular structures under axial impact loading, Eng. Struct. 182 (2019) 39–50, https://doi.org/10.1016/j.engstruct.2018.12.072.
[8] H. Nikkhah, A. Baroutaji, Z. Kazancı, A. Arjunan, Evaluation of crushing and energy absorption characteristics of bio-inspired nested structures, Thin-Walled Struct. 148 (2020) 106615.
[9] A. Baroutaji, M.D. Gilchrist, A.G. Olabi, Quasi-static, impact and energy absorption of internally nested tubes subjected to lateral loading, Thin-Walled Struct. 98 (2016) 337–350, https://doi.org/10.1016/j.tws.2015.10.001.
[10] H. Nikkhah, A. Baroutaji, A.G. Olabi, Crashworthiness design and optimisation of windowed tubes under axial impact loading, Thin-Walled Struct. 142 (2019) 132–148, https://doi.org/10.1016/J.TWS.2019.04.052.
[11] A. Eyvazian, M.K. Habibi, A.M. Hamouda, R. Hedayati, Axial crushing behavior and energy absorption efficiency of corrugated tubes, Mater. Des. 54 (2014) 1028–1038, https://doi.org/10.1016/j.matdes.2013.09.031.
[12] A. Baroutaji, M.D. Gilchrist, D. Smyth, A.G. Olabi, Analysis and optimization of sandwich tubes energy absorbers under lateral loading, Int. J. Impact Eng. 82 (2015) 74–88, https://doi.org/10.1016/j.ijimpeng.2015.01.005.
[13] A. Baroutaji, A.G. Olabi, Lateral collapse of short-length sandwich tubes compressed by different indenters and exposed to external constraints, Mater. Werkst. 45 (2014), https://doi.org/10.1002/mawe.201400236 n/a-n/a.
[14] F. Tarlochan, F. Samer, A.M.S. Hamouda, S. Ramesh, K. Khalid, Design of thin wall structures for energy absorption applications: enhancement of crashworthiness due to axial and oblique impact forces, Thin-Walled Struct. 71 (2013) 7–17, https://doi.org/10.1016/j.tws.2013.04.003.
[15] A. Baroutaji, M.D. Gilchrist, D. Smyth, A.G. Olabi, Crush analysis and multi-objective optimization design for circular tube under quasi-static lateral loading, Thin-Walled Struct. 86 (2015) 121–131, https://doi.org/10.1016/j.tws.2014.08.018.
[16] A. Baroutaji, E. Morris, A.G. Olabi, Quasi-static response and multi-objective crashworthiness optimization of oblong tube under lateral loading, Thin-Walled Struct. 82 (2014) 262–277, https://doi.org/10.1016/j.tws.2014.03.012.
[17] A. Niknejad, S.M. Elahi, S.A. Elahi, S.A. Elahi, Theoretical and experimental study on the flattening deformation of the rectangular brazen and aluminum columns, Arch. Civ. Mech. Eng. 13 (2013) 449–464, https://doi.org/10.1016/j.acme.2013.04.008.
[18] T. Tang, W. Zhang, H. Yin, H. Wang, Crushing analysis of thin-walled beams with various section geometries under lateral impact, Thin-Walled Struct. 102 (2016) 43–57, https://doi.org/10.1016/j.tws.2016.01.017.
[19] G.M. Nagel, D.P. Thambiratnam, Dynamic simulation and energy absorption of tapered thin-walled tubes under oblique impact loading, Int. J. Impact Eng. 32 (2006) 1595–1620, https://doi.org/10.1016/j.ijimpeng.2005.01.002.
[20] S.R. Reid, T.Y. Reddy, Static and dynamic crushing of tapered sheet metal tubes of rectangular cross-section, Int. J. Mech. Sci. 28 (1986) 623–637, https://doi.org/10.1016/0020-7403(86)90077-9.
[21] C.W. Isaac, Crushing response of circular thin-walled tube with non-propagating crack subjected to dynamic oblique impact loading, Int. J. Prot. Struct. 11 (2019) 41–68, https://doi.org/10.1177/2041419619849087.
[22] A.A.A. Alghamdi, Collapsible impact energy absorbers: an overview, Thin-Walled Struct. 39 (2001) 189–213, https://doi.org/10.1016/S0263-8231(00)00048-3.
[23] T. Wierzbicki, W. Abramowicz, On the crushing mechanics of thin-walled structures, J. Appl. Mech. 50 (1983) 727–734, https://doi.org/10.1115/1.3167137.
[24] W. Abramowicz, N. Jones, Dynamic progressive buckling of circular and square tubes, Int. J. Impact Eng. 4 (1986) 243–270, https://doi.org/10.1016/0734-743X(86)90017-5.
[25] W. Abramowicz, T. Wierzbicki, Axial crushing of multicorner sheet metal columns, J. Appl. Mech. 56 (1989) 113, https://doi.org/10.1115/1.3176030.
[26] W. Abramowicz, N. Jones, Transition from initial global bending to progressive buckling of tubes loaded statically and dynamically, Int. J. Impact Eng. 19 (1997) 415–437, https://doi.org/10.1016/S0734-743X(96)00052-8.
[27] G.M. Nagel, D.P. Thambiratnam, Computer simulation and energy absorption of tapered thin-walled rectangular tubes, Thin-Walled Struct. 43 (2005) 1225–1242, https://doi.org/10.1016/j.tws.2005.03.008.
[28] M.A. Guler, M.E. Cerit, B. Bayram, B. Gerçeker, E. Karakaya, The effect of geometrical parameters on the energy absorption characteristics of thin-walled structures under axial impact loading, Int. J. Crashworthiness 15 (2010) 377–390, https://doi.org/10.1080/13588260903488750.
[29] X. Zhao, G. Zhu, C. Zhou, Q. Yu, Crashworthiness analysis and design of composite tapered tubes under multiple load cases, Compos. Struct. 222 (2019) 110920, https://doi.org/10.1016/J.COMPSTRUCT.2019.110920.
[30] J. Zhang, D. Zheng, B. Lu, T. Zhang, Energy absorption performance of hybrid cross section tubes under oblique loads, Thin-Walled Struct. 159 (2021) 107133, https://doi.org/10.1016/J.TWS.2020.107133.
[31] G. Li, F. Xu, G. Sun, Q. Li, A comparative study on thin-walled structures with functionally graded thickness (FGT) and tapered tubes withstanding oblique impact loading, Int. J. Impact Eng. 77 (2015) 68–83, https://doi.org/10.1016/j.ijimpeng.2014.11.003.
[32] A. Arjunan, M. Demetriou, A. Baroutaji, C. Wang, Mechanical performance of highly permeable laser melted Ti6Al4V bone scaffolds, J. Mech. Behav. Biomed. Mater. (2020), https://doi.org/10.1016/j.jmbbm.2019.103517.
[33] A. Arjunan, J. Robinson, E. Al Ani, W. Heaselgrave, A. Baroutaji, C. Wang, Mechanical performance of additively manufactured pure silver antibacterial bone scaffolds, J. Mech. Behav. Biomed. Mater. 112 (2020) 104090, https://doi.org/10.1016/j.jmbbm.2020.104090.
[34] J. Robinson, A. Arjunan, A. Baroutaji, M. Martí, A. Tuñón Molina, Á. Serrano-Aroca, A. Pollard, Additive manufacturing of anti-SARS-CoV-2 Copper-Tungsten-Silver alloy, Rapid Prototyp. J. (2021), https://doi.org/10.1108/RPJ-06-2021-0131 ahead-of-p.
[35] A. Arjunan, S. Zahid, A. Baroutaji, J. Robinson, 3D printed auxetic nasopharyngeal swabs for COVID-19 sample collection, J. Mech. Behav. Biomed. Mater. (2020) 104175, https://doi.org/10.1016/j.jmbbm.2020.104175.
[36] A. Baroutaji, A. Arjunan, J. Robinsion, M. Ramadan, M.A. Abdelkareem, A.-G. Olabi, Metallic meta-biomaterial as biomedical implants, encycl, Smart Mater (2022) 70–80, https://doi.org/10.1016/B978-0-12-815732-9.00117-0.
[37] A. Baroutaji, A. Arjunan, M. Ramadan, J. Robinson, A. Alaswad, M. A. Abdelkareem, A.G. Olabi, Advancements and prospects of thermal management and waste heat recovery of PEMFC, Int. J. Thermofluids. 9 (2021) 100064, https://doi.org/10.1016/j.ijft.2021.100064.
[38] J. Robinson, A. Arjunan, A. Baroutaji, M. Stanford, Mechanical and thermal performance of additively manufactured copper, silver, and copper-silver alloys, Proc. Inst. Mech. Eng. Part L J. Mater. Des. Appl. (n.d.). https://wlv.openrepository.com/handle/2436/624360 (accessed September 30, 2021).
[39] A. Arjunan, A. Baroutaji, A. Latif, Acoustic behaviour of 3D printed titanium perforated panels, Results Eng. 11 (2021) 100252, https://doi.org/10.1016/J.RINENG.2021.100252.
[40] A. Arjunan, A. Baroutaji, J. Robinson, C. Wang, Characteristics of acoustic metamaterials, Encycl. Smart Mater. (2022) 35–45, https://doi.org/10.1016/B978-0-12-815732-9.00090-5.
[41] E. Cetin, C. Baykasoğlu, Energy absorption of thin-walled tubes enhanced by lattice structures, Int. J. Mech. Sci. 157–158 (2019) 471–484, https://doi.org/10.1016/j.ijmecsci.2019.04.049.
[42] A. Baykasoğlu, C. Baykasoğlu, E. Cetin, Multi-objective crashworthiness optimization of lattice structure filled thin-walled tubes, Thin-Walled Struct. 149 (2020) 106630, https://doi.org/10.1016/j.tws.2020.106630.
[43] E. Cetin, C. Baykasoğlu, Crashworthiness of graded lattice structure filled thin-walled tubes under multiple impact loadings, Thin-Walled Struct. 154 (2020) 106849, https://doi.org/10.1016/j.tws.2020.106849.
[44] N.T. Aboulkhair, M. Simonelli, L. Parry, I. Ashcroft, C. Tuck, R. Hague, 3D printing of Aluminium alloys: additive Manufacturing of Aluminium alloys using selective laser melting, Prog. Mater. Sci. 106 (2019), https://doi.org/10.1016/j.pmatsci.2019.100578.
[45] A. Baroutaji, A. Arjunan, J. Robinsion, M. Ramadan, M.A. Abdelkareem, A.-G. Olabi, Metamaterial for Crashworthiness Applications, Elsevier, 2021, https://doi.org/10.1016/B978-0-12-815732-9.00092-9.
[46] F. Trevisan, F. Calignano, M. Lorusso, J. Pakkanen, A. Aversa, E. Ambrosio, M. Lombardi, P. Fino, D. Manfredi, On the selective laser melting (SLM) of the AlSi10Mg alloy: process, microstructure, and mechanical properties, Materials 10 (2017) 76, https://doi.org/10.3390/ma10010076.
[47] M. Costas, D. Morin, M. de Lucio, M. Langseth, Testing and simulation of additively manufactured AlSi10Mg components under quasi-static loading, Eur. J. Mech. Solid. 81 (2020) 103966, https://doi.org/10.1016/J.EUROMECHSOL.2020.103966.

[48] S.E. Alkhatib, M.S. Matar, F. Tarlochan, O. Laban, A.S. Mohamed, N. Alqwasmi, Deformation modes and crashworthiness energy absorption of sinusoidally corrugated tubes manufactured by direct metal laser sintering, Eng. Struct. 201 (2019), https://doi.org/10.1016/j.engstruct.2019.109838.

[49] K. Hu, K. Lin, D. Gu, J. Yang, H. Wang, L. Yuan, Mechanical properties and deformation behavior under compressive loading of selective laser melting processed bio-inspired sandwich structures, Mater. Sci. Eng. 762 (2019) 138089, https://doi.org/10.1016/J.MSEA.2019.138089.

[50] Y. Zhang, T. Liu, H. Ren, I. Maskery, I. Ashcroft, Dynamic compressive response of additively manufactured AlSi10Mg alloy hierarchical honeycomb structures, Compos. Struct. 195 (2018) 45–59, https://doi.org/10.1016/J.COMPSTRUCT.2018.04.021.

[51] Y. Zhang, M. Lu, C.H. Wang, G. Sun, G. Li, Out-of-plane crashworthiness of bio-inspired self-similar regular hierarchical honeycombs, Compos. Struct. 144 (2016) 1–13, https://doi.org/10.1016/j.compstruct.2016.02.014.

[52] H. Yin, X. Huang, F. Scarpa, G. Wen, Y. Chen, C. Zhang, In-plane crashworthiness of bio-inspired hierarchical honeycombs, Compos. Struct. 192 (2018) 516–527, https://doi.org/10.1016/j.compstruct.2018.03.050.

[53] Z. Yang, Y. Yu, Y. Wei, C. Huang, Crushing behavior of a thin-walled circular tube with internal gradient grooves fabricated by SLM 3D printing, Thin-Walled Struct. 111 (2017) 1–8, https://doi.org/10.1016/J.TWS.2016.11.004.

[54] M. Zhao, F. Liu, G. Fu, D. Zhang, T. Zhang, H. Zhou, Improved mechanical properties and energy absorption of BCC lattice structures with triply periodic minimal surfaces fabricated by SLM, Materials 11 (2018) 2411, https://doi.org/10.3390/ma11122411.

[55] S.Y. Choy, C.N. Sun, K.F. Leong, J. Wei, Compressive properties of functionally graded lattice structures manufactured by selective laser melting, Mater. Des. 131 (2017) 112–120, https://doi.org/10.1016/j.matdes.2017.06.006.

[56] L. Zhang, S. Feih, S. Daynes, S. Chang, M.Y. Wang, J. Wei, W.F. Lu, Energy absorption characteristics of metallic triply periodic minimal surface sheet structures under compressive loading, Addit. Manuf. 23 (2018) 505–515, https://doi.org/10.1016/j.addma.2018.08.007.

[57] N. Novak, O. Al-Ketan, L. Krstulović-Opara, R. Rowshan, R.K. Abu Al-Rub, M. Vesenjak, Z. Ren, Quasi-static and dynamic compressive behaviour of sheet TPMS cellular structures, Compos. Struct. (2021) 113801, https://doi.org/10.1016/j.compstruct.2021.113801.

[58] EOS M 290 Technical Data, n.d, https://www.eos.info/en/additive-manufacturing/3d-printing-metal/eos-metal-systems/eos-m-290. (Accessed 26 September 2021).

[59] E.O.S. EOS, in: GmbH - Electro Optical Systems, Material Data Sheet EOS Aluminum AlSi10Mg, GPI Prototype Manuf. Serv., vol. 49, 2014, pp. 1–5. Fecha de última consulta 25/06/2021, https://gpiprototype.com/pdf/EOS_Aluminium_AlSi10Mg_en.pdf.

[60] W. Li, S. Li, J. Liu, A. Zhang, Y. Zhou, Q. Wei, C. Yan, Y. Shi, Effect of Heat Treatment on AlSi10Mg Alloy Fabricated by Selective Laser Melting: Microstructure Evolution, Mechanical Properties and Fracture Mechanism, 2016, https://doi.org/10.1016/j.msea.2016.03.088.

[61] L. Girelli, M. Tocci, M. Gelfi, A. Pola, Study of heat treatment parameters for additively manufactured AlSi10Mg in comparison with corresponding cast alloy, Mater. Sci. Eng. 739 (2019) 317–328, https://doi.org/10.1016/J.MSEA.2018.10.026.

[62] M. Giovagnoli, M. Tocci, A. Fortini, M. Merlin, M. Ferroni, A. Migliori, A. Pola, Effect of different heat-treatment routes on the impact properties of an additively manufactured AlSi10Mg alloy, Mater. Sci. Eng. 802 (2021) 140671, https://doi.org/10.1016/J.MSEA.2020.140671.

[63] M. Tang, P.C. Pistorius, Oxides, porosity and fatigue performance of AlSi10Mg parts produced by selective laser melting, Int. J. Fatig. 94 (2017) 192–201.

[64] G. Lu, T.X. Yu, Energy Absorption of Structures and Materials, Elsevier, 2003. https://books.google.com/books?hl=en&lr=&id=wRSkAgAAQBAJ&pgis=1. (Accessed 20 January 2016).

[65] A.S. Mohamed, O. Laban, F. Tarlochan, S.E. Al Khatib, M.S. Matar, E. Mahdi, Experimental analysis of additively manufactured thin-walled heat-treated circular tubes with slits using AlSi10Mg alloy by quasi-static axial crushing test, Thin-Walled Struct. 138 (2019) 404–414, https://doi.org/10.1016/j.tws.2019.02.022.

[66] Z. Tang, S. Liu, Z. Zhang, Analysis of energy absorption characteristics of cylindrical multi-cell columns, Thin-Walled Struct. 62 (2013) 75–84, https://doi.org/10.1016/j.tws.2012.05.019.

[67] N. Jones, Energy-absorbing effectiveness factor, Int. J. Impact Eng. 37 (2010) 754–765, https://doi.org/10.1016/j.ijimpeng.2009.01.008.

[68] A.A.A. Singace, Axial crushing analysis of tubes deforming in the multi-lobe mode, Int. J. Mech. Sci. 41 (1999) 865–890, https://doi.org/10.1016/S0020-7403(98)00052-6.

[69] G. Sun, Z. Wang, J. Hong, K. Song, Q. Li, Experimental investigation of the quasi-static axial crushing behavior of filament-wound CFRP and aluminum/CFRP hybrid tubes, Compos. Struct. 194 (2018) 208–225, https://doi.org/10.1016/J.COMPSTRUCT.2018.02.005.

[70] S.C.K. Yuen, G.N. Nurick, The energy-absorbing characteristics of tubular structures with geometric and material modifications: an overview, Appl. Mech. Rev. 61 (2008), 20802, https://doi.org/10.1115/1.2885138.